Multi-scaled porous Fe-N/C nanofibrous catalysts for the cathode electrodes of direct methanol fuel cells

Riguo Mei [a,b], *Jingjing Xi* [a,c], *Lei Ma* [a,b], *Liang An* [d], *Fang Wang* [a], *Hongyuan Sun* [a], *Zhongkuan Luo* [a,c], *Qixing Wu* [*,a]

[a] Shenzhen Key Laboratory of New Lithium-ion Batteries and Mesoporous Materials, College of Chemistry and Environmental Engineering, Shenzhen University, 3688 Nanhai Avenue, Nanshan District, Shenzhen, 518060, P.R. China.

[b] Key Laboratory of Optoelectronic Devices and Systems of Ministry of Education and Guangdong Province, College of Optoelectronic Engineering, Shenzhen University, Shenzhen 518060, P.R. China.

[c] Zhejiang California International NanoSystems Institute & Department of Materials Science and Engineering, Zhejiang University, 38 Zhe Da Road, Hangzhou, 310000, China

[d] Department of Mechanical Engineering, The Hong Kong Polytechnic University, Hung Hom, Kowloon, Hong Kong SAR, China.

Keywords: nanofibrous catalyst; oxygen reduction reaction; electrospinning; multi-scaled porous structure; direct methanol fuel cell.

[*]Corresponding Author: Tel: +86-755-26557393, E-mail: qxwu@szu.edu.cn (Qixing Wu)

Abstract: In the present work, a nanofibrous Fe-N/C catalyst with a multi-scaled porous structure is proposed and prepared via electrospinning a polyacrylonitrile (PAN) solution containing Fe^{3+} incorporated graphitic carbon nitride (Fe-g-C_3N_4). Physical and chemical characterizations confirm that micropores, mesopores and hollow-out macropores are co-existed in the Fe-N/C nanofibrous catalysts. The abundant micropores is beneficial for accommodating active sites, while the mesopores and hollow-out macropores can facilitate the supply of oxygen to the active surfaces. Moreover, due to the fibrous morphology of the catalyst, a 3D highly-porous electrode with well-established networks can be formed for facile transport of electrons and oxygen. The experimental results show that the Fe-N/C catalyst delivers a good activity towards oxygen reduction reaction (ORR) in acid media with a half-wave potential of 740 mV and an almost four-electron transfer process, high stability and excellent methanol tolerance. Furthermore, the as-prepared catalyst is used to fabricate the cathode of a direct methanol fuel cell, which yields a peak power density of 14.9 mW cm^{-2} with 1 M methanol solutions, dry air and an operating temperature of 70 ^{o}C.

1. INTRODUCTION

Direct methanol fuel cells (DMFC), the electrochemical devices utilizing methanol and oxygen as fuel and oxidant to directly convert chemical energy to electrical energy, have received tremendous interests due to their striking features, including high energy density, convenience in fuel handling and relatively compact system design. However, the wide-spread

commercialization of DMFCs is still impeded by a number of critical issues such as slow kinetics of methanol oxidation reaction (MOR), high cost of precious catalysts, methanol crossover and water flooding. Typically, Pt-based catalysts are the state-of-the-art cathode catalysts for oxygen reduction reaction (ORR) due to their excellent activity. Nevertheless, Pt-based catalysts are limited by high cost and the methanol poisoning effect. Hence, developing non-precious alternative ORR catalysts[1-7] is one of the most imperative tasks for the DMFC.

Iron and nitrogen doped carbon materials (Fe-N/C), have been proposed as potential alternatives for catalyzing ORR owing to its abundance, cost effectiveness, considerable activity, superior durability and excellent anti-poisoning ability against methanol[8-12]. Numerous efforts had been conducted to advance the Fe-N/C catalysts for fuel cell applications and a variety of highly active Fe-N/C catalysts were successfully synthesized and demonstrated with their ORR performance in alkaline media being comparable to Pt-based catalysts[13-16]. In terms of acidic ORR, the Fe–N/C catalyst seems much less satisfactory as it yields relatively poor activity and turnover frequency (TOF, ~0.4 s^{-1})[17, 18].

Previous and recent efforts have suggested that the porous structure of the Fe–N/C catalyst can play a pivotal role in its ORR performance[19-26]. Jaouen et al.[19] have found that most of active sites are accommodated by the micropores (<2 nm) of the Fe–N/C catalyst and the ORR activity can be significantly improved through introducing Fe-N_x centers into the micropores. In fact, for practical applications, hosting the active sites in the micropores is also exceptionally important: it can significantly increase the density of active sites or volumetric active surfaces in a fuel cell

electrode[20, 21], so that the electrode made of Fe–N/C catalysts can be maintained within a reasonable thickness of ~100 μm to reduce the polarization losses associated with the transport of proton, electron and oxygen. To increase the active sites in the micropores, Lefèvre et al.[20] used carbon black (Black Pearls 2000) with abundant micropores as the catalyst supports and employed the planetary ball-milling method to force the precursors and pore fillers into the micropores of carbon black in which the active sites were formed via pyrolysis under Ar or/and NH_3. In addition to carbon black, the zeolitic imidazolate framework (ZIF) was further introduced as a host for active sites due to its high nitrogen content and microporosity[21]. Apart from the micropores, the mesopores (2-50 nm) are also proposed to be crucial for presenting active surfaces and promoting the supply of reactants and removal of products to improve the accessibility of active sites[22-26]. To develop a mesoporous Fe-N/C catalyst, sacrificial templates such as mesoporous silica (SBA-15)[22], silica colloid[22], F-127[25] and ZIF-8[26] have usually been employed in the synthesis process. Liang et al.[22] used vitamin B12 and polyaniline-Fe complex as precursors and silica nanoparticles as the mesopore-forming agent, respectively; it was claimed that a plenty of mesopores with high specific surface areas was a key for distributing and exposing active sites as well as facilitating mass transport. With respect to the role of macropore (>50 nm), it is definitely not referred to hosting active sites due to its rather low volumetric surface area. However, the macropore can provide a highway for transporting oxygen from bulk to the vicinity of active sites and water removal[18], making it indispensable for improving the ORR performance.

To take advantages of various pores, hierarchically porous Fe–N/C catalysts have been designed and investigated in recent years[27-29]. By pyrolyzing Fe and N sources in the confined mesochannels of SBA-15, Kong et al.[27] successfully synthesized a highly porous Fe-N/C catalyst with Fe-N_x-embedded graphitic architectures, which showed an excellent catalytic reactivity for ORR. Li et al.[28] developed a meso/micro porous Fe–N/C catalyst with anodic aluminum oxide as the template and carbon nanotube as the support. To create a 3D Fe-N/C catalyst with hierarchical pores, Zuo et al.[29] introduced the thermalized triazine-based framework (TTF) as a template to form micro/meso/macro pores. In addition to the sacrificial templates, the electrospinning method, commonly used to fabricate tunable polymer nanofibers or membranes, is also introduced to the preparation of nanofibrous Fe-N/C catalysts for facile electron transfer[30-33] and the production of macro/meso-pores[18,33,34]. Jeong et al.[34] showed that the exposure of active sites insides the electrospun Fe-N/C nanofiber can be promoted by ball milling pulverization, which led to a significant increase in the reactivity. By adding ZIFs into the precursor solution, Shui et al.[18] created microporous Fe-N/C nanofibrous catalysts through electrospinning and the subsequent heat treatment. Due to the presence of numerous active micropores and interconnected macropores, an ultra-high volumetric catalytic activity of 450 A cm^{-3} was demonstrated.

In this work, a Fe-N/C nanofibrous catalyst with a multi-scaled porous structure was proposed and prepared via electrospinning a polyacrylonitrile (PAN) solution containing Fe^{3+} incorporated graphitic carbon nitride (Fe-g-C_3N_4) and subsequent heat and acid treatments. The

motivation of using g-C_3N_4 as the precursor was because of its high nitrogen content (60.9%) and its characteristic "nitrogen pots" which were beneficial for iron inclusion[35-37]. The preparation process is illustrated in Figure 1. It was expected that after the electrospinning, sheet-like Fe-g-C_3N_4 frameworks may be dispersed on/in both the surface and the interior of the PAN fibers. During pyrolysis, the Fe-g-C_3N_4 frameworks decomposed to form Fe-N active centers and release a variety of gas, leaving abundant micro/meso pores on the surface of carbon fibers and sparse hollow-out macropores probably resulted from the decomposition of large aggregates of Fe-g-C_3N_4 inside the PAN fiber. The prepared multi-scaled porous Fe-N/C nanofibrous catalyst with plenty of micro/meso/macro pores was evaluated by a series of physical, chemical and electrochemical characterizations and was used to fabricate the cathode electrode of a DMFC to investigate its practical performance.

2. EXPERIMENTAL SECTION

2.1 Preparation of porous Fe-N/C catalysts

Synthesis of g-C_3N_4: the spongy-like g-C_3N_4 (Figure S1) was prepared through a modified polycondensation method combined with solution mixing process[38]. Typically, 4.2 g melamine (99 wt. %, Aladdin) and 8.6 g cyanuric acid (98 wt. %, Aladdin) were dissolved in 300 mL and 500 mL hot water (80 ^oC), respectively, followed by mixing with these two solutions. After filtering, washing and drying, the g-C_3N_4 precursor was collected and treated at 550 ^oC in Argon for 5 h to obtain the g-C_3N_4.

Synthesis of Fe-N/C nanofibrous catalysts: the Fe-N/C nanofibers were prepared through

electrospinning followed by pyrolysis. Firstly, 0.350 g PAN (99 wt. %, Aladdin) was dissolved in 4.650 g N, N-dimethylformamide (DMF, 99 wt. %, Aladdin), followed by stirring for 12 h to obtain 7 wt. % PAN/DMF solution. Then, 0.165 g $FeCl_3$ (99.9 wt. % Aladdin) and 0.400 g g-C_3N_4 was dispersed in 3.150 g PAN/DMF solution. In order to incorporate Fe^{3+} into the mesoporous g-C_3N_4 frameworks (Figure S1), the polymer dispersion was sealed and stirred for 12 h. Then, the as-obtained yellow Fe-g-C_3N_4/PAN/DMF solution was electrospun with a voltage of 21 kV and a receiving distance of 10 cm. Subsequently, the Fe-g-C_3N_4/PAN nanofibrous precursor was pyrolyzed for 2 h at the temperatures of 700, 800, 900 and 1000 ^oC by a heating rate of 20 ^oC min^{-1} to attain Fe-N/C nanofibrous catalysts. For convenience, the Fe-N/C nanofibrous catalysts treated at 700, 800, 900 and 1000 ^oC were labeled as Fe-N/C-700, Fe-N/C-800, Fe-N/C-900 and Fe-N/C-1000, respectively. To improve the activity, Fe-N/C-900 was immersed in 0.5 M H_2SO_4 solution at 80 ^oC for 8 h. Then, the leached Fe-N/C-900 was pyrolyzed at 900 ^oC for 2 h again and denoted as Fe-N/C-900-LH.

2.2 Materials characterizations

The physical morphologies of prepared catalysts and electrodes were observed by using field emission scanning electron microscopy (FESEM, Hitachi SU-70) and transmission electron microscopy (TEM, Tecnai G2 Spirit 120 kV). The chemical compositions of catalysts were investigated by X-ray diffraction (XRD, D8 Advance, Bruker) tests, X-ray photoelectron spectroscopy (XPS, PHI5300, PE) and Raman spectroscopy (Renishaw Raman Microscope, 532 nm HeNe Laser). The specific surface area (SSA) and pore-size distribution of catalysts were

analyzed by a gas sorption instrument (V-Sorb 2800TP, BELL). Elemental analysis (Vario EL, Elementar) were used to obtain the elemental content of the in-house catalysts.

2.3 Electrocatalytic measurements

The fabrication of electrode for three-electrode tests was similar to our previous work[39]. The catalyst loading on the glassy carbon was maintained to be 0.8 mg cm^{-2} and the electrode made of commercial Pt/C (40 wt. % Pt, HiSPEC 4000) with a loading of 0.4 mg cm^{-2} was used for comparison. The electrocatalytic measurements were performed by a CHI 760d electrochemical station and RRDE-3A rotating disk electrode under room temperature. The counter and reference electrodes were Pt wire and Ag/AgCl electrode (saturated KCl solution), respectively. All potentials in this work were corrected by $E_{RHE}=E_{Ag/AgCl}+ E^{\theta}_{Ag/AgCl}+ 0.059$ pH and given versus reversible hydrogen electrode (RHE). The electrolyte was 0.5 M H_2SO_4 solution and was pre-purged and saturated by continuous flow of N_2 (99.99%) or O_2 (99.999%) to attain N_2- or O_2-saturated electrolyte. Cyclic voltammetry (CV) tests were conducted with a scan rate of 10 mV s^{-1} from 0 V to 1.2 V vs. RHE, whereas linear sweep voltammetry (LSV) was performed with rotating rates from 400 to 2500 rpm and a scan rate of 10 mV s^{-1}. The accelerated degradation tests (ADT) were performed in N_2-saturated electrolyte from 0.6 to 1.0 V vs. RHE and the scan rate was 50 mV s^{-1}. The methanol poisoning effect was studied by controlling the potential of the working electrode and rotating rate to be 0.4 V vs. RHE and 1600 rpm, respectively, followed by recording the change in the current after deliberate addition of 10 mL pure methanol

into the electrolyte. The measured ORR currents in O_2-saturated electrolyte were corrected by subtracting their respective currents in N_2-saturated electrolyte.

2.4 Fuel cell assembly and test

The catalyst ink used for fabricating the fuel cell electrode was consisted of Fe-N/C-900-LH catalyst and Nafion ionomer with a mass ratio of 1:1 and the processing procedure was similar to our previous work[40]. The deposition of the catalysts was by ultrasonically spraying the catalyst ink onto a microporous layer coated carbon paper (Toray 060) and the loading of Fe-N/C-900-LH catalyst was 5.0 mg cm^{-2}. The anode electrode was the commercially available electrode from Johnson Matthey and the PtRu metal loading was 2 mg cm^{-2}. The membrane electrode assembly (MEA) was formed by sandwiching a Nafion 212 membrane between two electrodes through hot pressing at 3.2 MPa and 140 ^oC for 3 min.

The prepared MEA was assembled with a DMFC hardware, which consisted of two graphite blocks (Poco Graphite) machined with single-pass serpentine flow fields (the channel depth and width were 1 mm and 0.6 mm, respectively), two gold-coated current collectors and two aluminum end plates. A fuel cell testing system (Arbin BT-5HC) was used for measuring the DMFC polarization curves. During performance tests, the anode and cathode of the DMFC were fed by methanol solution at 2.5 mL min^{-1} and dry compressed air at 100 sccm, respectively. The operating temperatures and methanol concentrations under investigation were ranged from 30 to 70 ^oC and from 1 to 8 M, respectively.

3. RESULTS AND DISCUSSION

3.1 Physical and chemical characterizations

As shown in Figure 2a and 2b, the prepared catalysts are nanofibrous with fiber diameters of 260 ±80 nm (Figure S2) and sparse hollow-out macropores are clear to observe in the magnified SEM image (Figure 2b). Such macropores are also confirmed by a close look at the single nanofibrous catalyst in Figure 2c. These relatively large macropores with hundreds of nanometers in size are beneficial for providing additional pathways for oxygen supply and water removal. In addition, as shown in Figure 2c and 2d, few Fe nanoparticles are also found to be embedded in the graphitic carbon, somewhat increasing the electrical conductivity of the catalysts and activate the graphitic carbon shell to facilitate ORR[40]. The typical HAADF-STEM image (Figure 2e) of Fe-N/C-900-LH also shows that few Fe nanoparticles were presented in the carbon nanofiber, which is hollow and almost transparent. Figure 2f shows the STEM image of selected area and its corresponding elemental mapping images of C, N and Fe. It can be seen that the distributions of C, N and Fe elements are generally matched with the shape of Fe-N/C nanofiber, somewhat suggesting the well dispersion of active sites since Fe-N_x and N-doped carbon are mainly responsible for accelerating ORR[41-45].

The effect of carbonization temperature on the physical structure and chemical composition of Fe-N/C nanofibers was investigated by SEM, XRD, XPS, elemental analysis, Raman spectroscopy and N_2 adsorption/desorption isotherms. Clearly, the apparent morphologies of various samples (Figure S3) seem almost unaffected by carbonization temperatures. Figure 3a

shows the XRD patterns of various samples, and the enlarged image with standard XRD patterns of main species is presented in Figure S4. It is found that the diffraction peaks of C (002) at 26.3° strengthen with increasing carbonization temperature from 700 to 1000 °C, indicating a higher degree of graphitization at high temperatures. In addition, it is found that the carbonization temperature influences the presences of particle phases in Fe-N/C nanofibers: the diffraction peaks of Fe_3N and Fe_3C tend to fade away by increasing the temperature from 700 to 1000 °C, whereas the peaks of $Fe_{15.1}C$ and Fe seem to be strengthened at high temperatures (⩾800 °C). Moreover, it worth mentioning that except for few embedded Fe in the carbon, most of the unstable Fe is removed after acid leaching and a second pyrolysis, which can be confirmed by the weakening of the diffraction peak intensity (Figure S5). To characterize the elemental composition of the prepared catalysts, XPS survey is performed and the result (Figure 3b) shows that four elements including C, N, O and Fe exist in Fe-N/C nanofibrous catalysts. The graphitization of pyrolyzed carbon for Fe-N/C nanofibers is determined by Raman spectroscopy. Figure 3c shows that the peak intensity ratios (I_D/I_G) is smaller at higher pyrolysis temperature, which suggests that the graphitization of Fe-N/C nanofibers increases with an increase of carbonization temperature, in a good agreement with the results of XRD. Meanwhile, it is reasonable to see that Fe-N/C-900-LH delivers a higher level of graphitization than does Fe-N/C-900 simply due to second pyrolysis. Additionally, from the high-resolution C1s spectra in Figure S6, one can estimate the percentage of sp^2-hybridized carbon atoms and further confirmed that a higher carbonization temperature and a second pyrolysis are favorable for graphitization.

Table 1. The analysis on pore structure of various Fe-N/C nanofibrous catalysts.

Samples	micropore	mesopore	macropore	SSA_{BET}	pore volume
	peak pore diameter (Å)	mean pore diameter (nm)	mean pore diameter (nm)	$m^2\ g^{-1}$	$cm^3\ g^{-1}$
Fe-N/C-700	-, 6.5	14.8	86.1	142	0.795
Fe-N/C-800	5.1, 6.4	10.9	84.7	319	0.869
Fe-N/C-900	5.4, 6.6	10.2	88.0	343	0.875
Fe-N/C-1000	5.4, 6.4	8.7	86.5	372	0.990
Fe-N/C-900-LH	5.9, 7.1	9.0	90.2	392	0.915

The multi-scaled porous structures of the catalysts are evaluated by N_2 adsorption/desorption isotherms and results are shown in Figure 3d. The micropore size distributions and macro/mesopore size distributions of Fe-N/C nanofibrous catalysts are estimated by Horvath-Kawazoe (HK) method and Barrett-Joyner-Halenda (BJH) method, respectively. Obviously, as evident in Figure 3e and 3f, the Fe-N/C nanofibrous catalysts consist of micro/meso/macro pores. The formation of micro/meso/macro pores is rather complicated during thermal processing and previous investigations have shown that the precursors[19-29,46], pyrolysis temperature[19,37,47] and time of heat treatment[19] as well as atmosphere[20,21] play critical roles in the pore structure. It is noted in Table 1 that the mean pore sizes of micropores, mesopores and macropores in our samples are about 0.6, 10 and 85 nm, respectively. Meanwhile, it is observed that elevating the pyrolysis temperature from 700 ^oC to 1000 ^oC leads to an increase of the SSA_{BET}, in agreement with the work by Tao et al.[47]. It is noted in Table 1 that the mean pore diameter of the mesopores tends to decrease at elevated pyrolysis temperatures, and hence we speculate that the increases of SSA_{BET} and pore volume is likely caused by the formation of additional nanopores during pyrolysis. Furthermore, it is noted that both the

SSA_{BET} and pore volume of Fe-N/C-900 are increased by acid leaching and a second pyrolysis, probably due to the removal of impurities. It is worth mentioning that the SSA_{BET} may be further increased by a pyrolysis under NH_3 atmosphere[20,21] and the pore size distribution may be more uniform by introducing micro/meso pore-forming agents into the precursor solution[18, 22, 26].

As the N content and the N-containing species play important roles in rendering active sites for ORR, elemental analysis and high-resolution N 1s spectra of various catalysts pyrolyzed at temperatures from 700 to 1000 °C were conducted for in-depth analysis. As shown in Table S1, the total N content is found to be decreased from 10.45 wt. % to 2.32 wt. % with increasing temperature from 700 ^{o}C to 1000 ^{o}C, mainly due to the accelerated decomposition of N-containing species at a higher temperature. After acid leaching and a subsequent pyrolysis, the total N content slightly decreases from 4.72 wt. % (Fe-N/C-900) to 4.05 wt. % (Fe-N/C-900-LH). Figure 4 shows that all Fe-N/C nanofibrous catalysts exhibit four similar peaks at about 398.3, 399.5, 400.8 and 402.3 eV, which correspond to pyridinic N, pyrrolic N, graphitic N and oxidized N, respectively. The high-resolution N 1s spectra are quantitatively deconvolved to estimate the contents of different N species (Table S2). It can be seen that the total contents of pyridinic N and pyrrolic N generally decrease by increasing the carbonization temperature, whereas the graphitic N content increases at elevated temperatures due to a higher degree of graphitization. In addition, it is understood that after acid leaching and a second pyrolysis, the percentage of graphitic N in Fe-N/C-900 is observed to be increased[48]. As the graphitic N may prefer to bind with iron to create the Fe-N_x active centers[45, 49], a high graphitic N content of Fe-

N/C-900-LH is desirable in terms of improving ORR activity.

To gain some understanding on the Fe content and its bonding states in our samples, a high-resolution Fe XPS analysis is shown in Figure 5. It is noted that both Fe^{2+} and Fe^{3+} species are presented in all the prepared samples. The peaks located at 710.9 eV and 714.3 eV can be assigned to $2p_{3/2}$ orbitals of Fe^{2+} and Fe^{3+} species and the peaks at 723.4 eV and 725.3 eV are corresponded to the $2p_{1/2}$ orbitals of Fe^{2+} and Fe^{3+} species, respectively. The peak at 719.6 eV is attributed to satellite peak of Fe and no detectable signal of Fe^0 is obtained at 707 eV, indicating that Fe^0 species are most likely embedded in the inner of carbon nanofibers. Meanwhile, the contents of total Fe, Fe^{2+} and Fe^{3+} obtained from XPS data tend to decrease with an increase of pyrolysis temperature (Figure 5f), which is consistent with previous observations[50,51] and might be resulted from the coverage by a thicker carbon layer at higher temperatures[51]. More importantly, it is found that the ratio of Fe^{2+} to Fe^{3+} of Fe-N/C-900-LH is 2.0, higher than that of Fe-N/C-900 (1.42). Since Fe^{2+}-N_4 moieties may contribute to active centers as suggested by recent works[52, 53], a larger content of Fe^{2+} species in Fe-N/C-900-LH is expected to facilitate ORR performance.

3.2 Electrocatalytic measurement

Figure 6a presents the CV curves for various catalysts in N_2- or O_2- saturated electrolyte. Except for Fe-N/C-700, other prepared catalysts show obvious ORR peaks in the presence of O_2 and no observable peak in the N_2-saturated environment. Moreover, compared with other catalysts, Fe-N/C-900-LH delivers the highest onset potential and the largest peak current. As shown in Figure

6b and Table 2, the diffusion-limited current densities and half-wave potentials for Fe-N/C-700, Fe-N/C-800, Fe-N/C-900 and Fe-N/C-1000 are 1.40, 3.41, 3.60, 2.41 mA cm^{-2} and 0.58, 0.64, 0.69, 0.69 V, respectively, indicating that the ORR activity firstly increases and then decreases with an increase in carbonization temperature. The improvement in the ORR performance can be attributed to the increase in the SSA (Table 1) and the formation of active sites (Table S2 and Figure 5) when elevating the temperature from 700 to 900 ^{o}C. However, further increasing the carbonization temperature to 1000 ^{o}C can lead to substantial loss of N-containing active sites (Table S1), which in turn counteracts the positive effect of the increase in the SSA at 1000 ^{o}C. Hence, Fe-N/C-900 exhibits the best ORR performance. It is worth mentioning that, after acid leaching and a second pyrolysis, Fe-N/C-900-LH yields a significantly improved ORR activity: a half-wave potential of 0.74 V and a diffusion-limited current density of 4.28 mA cm^{-2} under 1600 rpm, which are somehow comparable to previous advanced catalysts (Tables S3).

To study the intrinsic ORR activity, a series of LSVs for Fe-N/C-900-LH was collected with various rotating rates and results are shown in Figure 6c. Obviously, the diffusion-limiting current density is increased by enhancing the rotation rates, suggesting diffusion-limiting kinetics of ORR. Moreover, it is notable that the LSV curve at 400 rpm shows an small ORR peak, which is absent at higher rotation rates. This could be interpreted as diffusion-limiting process for solid phase diffusion or in-plane diffusion when the catalyst loading is relatively high[54]. The number of electron transfer (n) is estimated from LSV by using the Koutechy-Levich equation. The detailed calculation is available in the supplementary materials. As noted in Figure 6d, the

electron transfer numbers are varied with potentials and its mean value of Fe-N/C-900-LH is 3.85, much larger than that of Fe-N/C-900 (Figure S8), which indicates the necessity of acid and subsequent heat treatment. In addition, from the Tafel plots shown in Figure S7, it is noted that Fe-N/C-900-LH presents a similar slope (79.6 mV dec^{-1}) as Pt/C, suggesting a similar ORR mechanism. Generally, the Tafel slope of 79.6 mV dec^{-1} can be attributed to Temkin adsorption of O at a higher coverage of the surface O species[55].

Table 2. The characteristic parameters of ORR for various catalysts.

Samples	onset potential (V vs. RHE)	half-wave potential (V vs. RHE)	J_d at 1600 rpm (mA cm^{-2})
Fe-N/C-700	0.75	0.58	1.40
Fe-N/C-800	0.77	0.64	3.41
Fe-N/C-900	0.79	0.69	3.60
Fe-N/C-1000	0.78	0.69	2.41
Fe-N/C-900-LH	0.83	0.74	4.28
Pt/C	0.87	0.79	4.27

The short-term stability of Fe-N/C-900-LH is investigated by ADT. As indicated in Figure 6e, the LSV curve of Fe-N/C-900-LH almost unchanged, whereas the commercial Pt/C shows obvious declines in the half-wave potential and limiting current density. The limiting current density of Fe-N/C-900-LH remains 99.4% after 10000 cycles, much better than that of the Pt/C (94.5%). Moreover, the half-wave potentials of Fe-N/C-900-LH and Pt/C negatively shift 6 and 32 mV after ADT, respectively. The excellent stability of Fe-N/C-900-LH may arise not only from the stable Fe-N_x moieties but also from the stubborn structure of the nanofibers. The methanol tolerance ability is highly desirable for cathode catalysts of DMFCs. To investigate this ability of Fe-N/C-900-LH, pure methanol (24.7 M) is deliberately added into the electrolyte

(resulting in a methanol concentration of 3M) to observe the poisoning effect of methanol during chronoamperometric tests. It is seen in Figure 6f, the current density of Fe-N/C-900-LH is nearly unaffected after introduction of methanol, whereas the current density of Pt/C catalyst rapidly drops by 53.5%, suggesting that Fe-N/C-900-LH possesses a much higher anti-poisoning ability than does the Pt/C. As demonstrated by D. Sebastián et al.[12], the adsorption energy of oxygen on Fe-N_4 and Fe-N_2C_2 sites are much more negative than those of methanol, and hence oxygen rather than methanol may preferentially be adsorbed by Fe-N/C catalyst to proceed ORR even in the presence of methanol.

3.3 DMFC test

The practical performance of Fe-N/C-900-LH was investigated by a single DMFC. Figure 7 presents the physical morphology of the cathode catalyst layer formed by Fe-N/C-900-LH and Nafion ionomers and its corresponding elemental mapping. The low magnified SEM image (Figure 7a and Figure S9) shows that the catalyst layer of Fe-N/C-900-LH is relatively flat without any visibly large cracks or holes. Nevertheless, from the high magnified SEM image (Figure 8a), it is clear that the catalyst layer is indeed constructed by numerous porous nanofibrous catalysts with randomly networking (packing) to present abundant interconnected macropores (~5 μm), which may be helpful for the transport of oxygen through the catalyst layer to the deep active sites (i.e., in the vicinity of membrane/electrode interface) to enhance the unitization of catalysts. From the cross-sectional SEM images (Figure 8b) of the catalyst layer, one can see that the catalyst layer is a 3D porous structure with loosely packing of nanofibrous

catalysts and its thickness is about 110 μm. Such a large thickness is arisen from a high catalyst loading of 5 mg cm^{-2} and a large Nafion content of 50 wt. % in the electrode. It is reported that the loading of Fe-N/C and Nafion should be high enough to ensure a considerable fuel cell performance, because the active sites per unit catalyst mass of Fe-N/C is substantially lower than that of Pt-based catalysts and additional Nafion ionomer should be introduced for the forming the triple phase boundaries[56]. It is worth mentioning that a thick catalyst layer is generally undesirable since it will pose transport issues for oxygen, proton and electron: a longer pathway has to pass before reaching the triple phase boundary. Due to the unique 3D porous structure formed by nanofibrous Fe-N/C catalyst, it is assumed that the transport problem of thick catalyst layer is somehow alleviated. In addition, the uniform distribution of elemental C, N and Fe mappings in Figure 7(b-d) indicates a well dispersion of Fe-N/C nanofibrous catalysts within the catalyst layer. In addition to the dispersion of catalyst, the Nafion ionomers is found to be uniformly distributed into the catalysts, which is indirectly reflected by the mappings of element S (Figure 7e) that only exists in the form of sulfonic acid group in Nafion ionomer. The well distribution of Nafion ionomers is critically important as it helps to set up the triple phase boundaries for ORR and provides sufficient pathways for transferring protons into (or out from) the catalysts layer. Figure 7f presents the contents of main elements in the catalyst layer. The measured contents of C, N, Fe and S are 74%, 1%, 6% and 1%, respectively, well matched with the calculated values.

Figure 8c shows the DMFC performance at the operating temperatures from 30 to 70 ^{o}C. It is seen that the DMFC performance improves with an increase in the temperature: the peak power densities at 30, 50 and 70 ^{o}C are 5.2, 10.0 and 14.9 mW cm^{-2}, respectively. The enhanced performance is due to an enhanced reactivity of anode and cathode catalysts, an increase in the proton conductivity of Nafion and a promotion of mass transfer at elevated temperatures. According to recent literature[7,10,57-59], the peak power densities of DMFCs with Fe-N/C cathode catalysts are ranged from 5.8-25.0 mW cm^{-2} with pure oxygen as the cathode reactant, and hence the performance of the DMFC in this work is reasonable since air, instead of oxygen, is used as cathode oxidant. Figure 8d presents the DMFC performance with various methanol concentrations from 1 to 8 M. It is observed that the DMFC performance only slightly decreases with increased methanol concentrations; the peak power densities are 14.9, 13.4, 12.3 and 11.0 mW cm^{-2}, respectively, with 1, 2, 4 and 8 M methanol solutions. For a thin proton conducting membrane (i.e., Nafion 212), methanol crossover is primarily driven by diffusion and it is expected to dominate under the open circuit condition as the methanol concentration in the anode electrode is highest due to no MOR consumption. Hence, the open circuit voltage can reflect the degree of methanol poisoning to some extent. As shown in the inset of Figure 8d, the measured open circuit voltages are found to be almost the same (~580 mV) with various methanol concentrations of 2, 4 and 8 M, which suggests that the deleterious effect of methanol poisoning is significantly alleviated by using the Fe-N/C nanofiber as the cathode catalyst. Our result is somehow consistent with the previous work[57], in which it is found that the performance of the

DMFC with Fe-N/C catalysts decreases with an increase of methanol concentration from 2 M to 10 M but it increases with methanol concentration from 1 M to 2 M. The reason leading to this discrepancy may be that our anode diffusion layer is much thinner, thereby less susceptible to transport loss (i.e., no severe concentration polarization in the anode catalyst layer even for 1 M methanol). Based on the above DMFC performance tests, it can be concluded that the multi-scaled porous Fe-N/C nanofiber is a promising candidate as the DMFC cathode catalyst in terms of replacing precious Pt-based catalysts.

4. CONCLUSIONS

To sum up, a multi-scaled porous Fe-N/C nanofibrous catalyst for ORR were successfully synthesized via electrospinning, acid leaching and pyrolysis and it was applied to a DMFC for practical evaluation. Materials characterizations of the prepared catalysts confirmed the presence of abundant miro/meso/marcopores and active sites for ORR. Among all the prepared samples, the one pyrolyzed at 900 ^{o}C with subsequent acid and heat treatments, Fe-N/C-900-LH, can deliver a half-wave potential of 740 mV accompanied by a nearly 4e^{-} process towards ORR. By applying the nanofibrous Fe-N/C-900-LH to the cathode of a DMFC, a 3D porous electrode with interconnected pores was constructed and the DMFC yielded a peak power density of 14.9 mW cm^{-2} at 70 ^{o}C with a good tolerance against methanol. Although promising, there exists plenty of room for further improving the performance of the DMFC based on nanofibrous Fe-N/C catalysts: optimizing the precursor compositions, electrospinning parameters and pyrolysis

processes to facilitate the formation of active sites, adding micropore formers to increase SSA and developing novel techniques to impregnate Nafion into the electrode with a lower weight content to ensure a facile transport of reactants, products and protons.

ASSOCIATED CONTENT

Supporting Information.

SEM, TEM, XRD, XPS, FTIR and N_2 adsorption−desorption curve of spongy-like g-C_3N_4, SEM image of Fe-N/C-900-LH and its corresponding fiber diameter distribution, SEM images of Fe-N/C-700, Fe-N/C-800, Fe-N/C-900 and Fe-N/C-1000, XRD patterns of Fe-N/C-900 (before acid leaching), Fe-N/C-900-AL (after acid leaching) and Fe-N/C-900-LH, high-resolution C 1s spectra of various Fe-N/C catalysts, Tafel plots of various catalysts, LSV curves, electron transfer number and Tafel plots of Fe-N/C-900, and SEM images of the catalyst layer, element analysis results and the contents of different N species and comparison of ORR performance with various iron-based catalysts in acidic media.

ACKNOWLEDGMENTS

This work was supported by the National Natural Science Foundation of China (No. 51306125), China Postdoctoral Science Foundation (2016M602516), Shenzhen Science and Technology Fund (JCYJ20150324141711693) and Natural Science Foundation of SZU (No. 827-000015).

REFERENCES

1. J. K. Dombrovskis and A. E. C. Palmqvist, *Fuel Cells*, **68**, 1325 (2016).
2. C. Zhu, H. Li, S. Fu, D. Du and Y. Lin, *Chemical Society reviews*, **45**, 517 (2016).
3. P. Zamani, D. C. Higgins, F. M. Hassan, X. Fu, J. Y. Choi, M. A. Hoque, G. Jiang and Z. Chen, *Nano Energy*, **26**, 267 (2016).
4. Y. Qian, P. Du, P. Wu, C. Cai and D. F. Gervasio, *J Phys Chem C*, **120**, 9884 (2016).
5. J. Wei, Y. Liang, Y. Hu, B. Kong, J. Zhang, Q. Gu, Y. Tong, X. Wang, S. P. Jiang and H. Wang, *Angewandte Chemie International Edition*, **128**, 12658 (2016).
6. L. Gu, L. Jiang, X. Li, J. Jin, J. Wang and G. Sun, *Chinese J Catal*, **37**, 539 (2016).
7. M. Xiao, J. Zhu, L. Feng, C. Liu and W. Xing, *Adv Mater*, **27**, 2521 (2015).
8. L. Yang, Y. Su, W. Li and X. Kan, *J Phys Chem C*, **119**, 11311 (2015).
9. Y. C. Wang, Y. J. Lai, L. Song, Z. Y. Zhou, J. G. Liu, Q. Wang, X. D. Yang, C. Chen, W. Shi and Y. P. Zheng, *Angewandte Chemie*, **127**, 10045 (2015).
10. Y. Hu, J. Zhu, Q. Lv, C. Liu, Q. Li and W. Xing, *Electrochimica Acta*, **155**, 335 (2015).
11. W. Yang, X. Liu, L. Chen, L. Liang and J. Jia, *Chem Commun*, **53**, 4034 (2017).
12. D. Sebastian, A. Serov, I. Matanovic, K. Artyushkova, P. Atanassov, A. Arico and V. Baglio, *Nano Energy*, **34**, 195 (2017).
13. L. Lin, Q. Zhu and A.-W. Xu, *J Am Chem Soc*, **136**, 11027 (2014).
14. Q. X. Lai, Q. W. Gao, Q. Su, Y. Y. Liang, Y. X. Wang and Z. Yang, *Nanoscale*, **7**, 14707 (2015).
15. J. Sanetuntikul and S. Shanmugam, *Nanoscale*, **7**, 7644 (2015).
16. Q. Li, H. Y. Pan, D. Higgins, R. G. Cao, G. Q. Zhang, H. F. Lv, K. B. Wu, J. Cho and G. Wu, *Small*, **11**, 1443 (2015).
17. N. R. Sahraie, U. I. Kramm, J. Steinberg, Y. Zhang, A. Thomas, T. Reier, J. P. Paraknowitsch and P. Strasser, *Nature Communications*, **6**, 8618 (2015).
18. J. Shui, C. Chen, L. Grabstanowicz, D. Zhao and D. J. Liu, *Proceedings of the National Academy of Sciences*, **112**, 10629 (2015).
19. F. Jaouen, M. Lefèvre, J.-P. Dodelet and M. Cai, *The Journal of Physical Chemistry B*, **110**, 5553 (2006).
20. M. Lefèvre, E. Proietti, F. Jaouen and J.-P. Dodelet, *Science*, **324**, 71 (2009).
21. E. Proietti, F. Jaouen, M. Lefèvre, N. Larouche, J. Tian, J. Herranz and J.-P. Dodelet, *Nature communications*, **2**, 416 (2011).
22. H.W. Liang, W. Wei, Z.S. Wu, X. Feng, K. Müllen, *J. Am. Chem. Soc.* **135** 16002 (2013).
23. X.H.Yan, B.Q. Xu, *J. Mater. Chem. A*, **2**, 8617 (2014).
24. G.A. Ferrero, K. Preuss, A. Marinovic, A.B. Jorge, N. Mansor, J. Dan, A.B. Fuertes, M. Sevilla, M.M. Titirici, *ACS N*ano, **10**, 5922 (2016).
25. J.Liang, R.F. Zhou, X.M. Chen, Y.H. Tang, S.Z. Qiao, *Adv. Mater.*, **26**, 6074 (2014).
26. M. Thomas, R. Illathvalappil, S. Kurungot, B.N. Nair, A.A.P. Mohamed, G.M.

Anilkumar, T. Yamaguchi, U. Hareesh, *ACS Appl. Mater. Interfaces*, **8**, 29373 (2016).

27. A. Kong, X. Zhu, Z. Han, Y. Yu, Y. Zhang, B. Dong and Y. Shan, *Acs Catal*, **4**, 1793 (2014).

28. J. C. Li, P. X. Hou, C. Shi, S. Y. Zhao, D. M. Tang, M. Cheng, C. Liu and H. M. Cheng, *Carbon*, **109**, 632 (2016).

29. Q. Zuo, P. Zhao, W. Luo and G. Cheng, *Nanoscale*, **8**, 14271 (2016).

30. P. Zamani, D. Higgins, F. Hassan, G. Jiang, J. Wu, S. Abureden and Z. Chen, *Electrochimica Acta*, **139**, 111 (2014).

31. N. Wu, Y. Wang, Y. Lei, B. Wang, C. Han, Y. Gou, Q. Shi and D. Fang, *Sci Rep-Uk*, **5**, 17396 (2015).

32. J. Yin, Y. Qiu and J. Yu, *Electrochem Commun*, **30**, 1 (2013).

33. X. Yan, K. Liu, X. Wang, T. Wang, J. Luo and J. Zhu, *Nanotechnology*, **26**, 165401 (2015).

34. B. Jeong, D. Shin, H. Jeon, J. D. Ocon, B. S. Mun, J. Baik, H. J. Shin and J. Lee, *Chemsuschem*, **7**, 1289 (2014).

35. G. Algara-Siller, N. Severin, S. Chong, Y. Bjorkman, R. Palgrave, A. Laybourn, M. Antonietti, Y. Khimyak, A. Krasheninnikov, J. Rabe, U. Kaiser, A. Cooper, A. Thomas, M. Bojdys, *Angew. Chem. Int. Edit.*, **53**, 7450 (2014).

36. Y.T. Gong, M.M. Li, Y. Wang, *ChemSusChem*, **8**, 931 (2015).

37. M. Q. Wang, W. H. Yang, H. H. Wang, C. Chen, Z. Y. Zhou and S. G. Sun, *Acs Catal*, **4**, 3928 (2014).

38. R. G. Mei, L. Ma, L. An, F. Wang, J.J. Xi, H.Y. Sun, Z.K. Luo, Q.X. Wu, *J Electrochem Soc*, **164**, F354(2017).

39. J.J. Xi, F. Wang, R.G. Mei, Z.J. Gong, X.P. Fan, H. Yang, L. An, Q.X. Wu and Z.K. Luo, *RSC Adv*, **6**, 90797 (2016).

40. H. Jiang, Y. Yao, Y. Zhu, Y. Liu, Y. Su, X. Yang and C. Li, *Acs Appl Mater Inter*, **7**, 21511 (2015).

41. A. Serov, K. Artyushkova and P. Atanassov, *Adv Energy Mater*, **4**, 919 (2014).

42. F. J. Pérez-Alonso, C. Domínguez, S. A. Al-Thabaiti, A. O. Al-Youbi, M. A. Salam, A. A. Alshehri, M. Retuerto, M. A. Peña and S. Rojas, *J Power Sources*, **327**, 204 (2016).

43. U. Tylus, Q. Jia, H. Hafiz, R. J. Allen, B. Barbiellini, A. Bansil and S. Mukerjee, *Applied Catalysis B Environmental*, **198**, 318 (2016).

44. G. McCool, C. Ma, X. Yuan, Z.F. Ma, S. Mukerjee, Q. Jia, *Energy & Environmental Science*, **9**, 2418 (2016).

45. D. Guo, R. Shibuya, C. Akiba, S. Saji, T. Kondo and J. Nakamura, *Science*, **351**, 361 (2016).

46. Z. Li, G. Li, L. Jiang, J. Li, G. Sun, C. Xia, F. Li, *Angew. Chem. Int. Edit.*, **54**, 1494 (2015).

47. G. Tao, L. Zhang, L. Chen, X. Cui, Z. Hua, M. Wang, J. Wang, Y. Chen, J. Shi, *Carbon*,

86, 108 (2015).

48. J. J. Li, Y. M. Zhang, X. H. Zhang, J. C. Han, Y. Wang, L. Gu, Z. H. Zhang, X. J. Wang, J. K. Jian, P. Xu and B. Song, *Acs Appl Mater Inter*, **7**, 19626 (2015).

49. H. B. Yang, J. Miao, S. F. Hung, J. Chen, H. B. Tao, X. Wang, L. Zhang, R. Chen, J. Gao and H. M. Chen, *Science Advances*, **2** , e1501122 (2016).

50. R. Kothandaraman, V. Nallathambi, K. Artyushkova, S.C. Barton, *Appl. Catal. B-Environ.*, **92(1-2)**, 209 (2009).

51. K.P. Singh, E.J. Bae, J.S. Yu, *J. Am. Chem. Soc.*, **137**, 3165 (2015)

52. U. I. Kramm, M. Lefevre, N. Larouche, D. Schmeisser and J. P. Dodelet, *J Am Chem Soc*, **136**, 978 (2014).

53. A. Zitolo, V. Goellner, V. Armel, M.T. Sougrati, T. Mineva, L. Stievano, E. Fonda, F. Jaouen, *Nat. Mater.*, **14**, 937 (2015).

54. M. Zhou, C. Yang and K. Y. Chan, *Adv Energy Mater*, **4**, 1400840 (2014).

55. D. W. Shoesmith, J. S. Betteridge and W. H. Hocking, *J Electroanal Chem*, **406**, 69 (1996).

56. J. C. Park, S. H. Park, W. C. Min, H. C. Chang, B. K. Kho and S. I. Woo, *J Power Sources*, **286**, 166 (2015).

57. E. Negro, A. H. A. M. Videla, V. Baglio, A. S. Aricò, S. Specchia and G. J. M. Koper, *Applied Catalysis B Environmental*, **s166–167**, 75 (2015).

58. D. Sebastián, A. Serov, K. Artyushkova, J. Gordon, P. Atanassov, A. S. Aricò and V. Baglio, *ChemSusChem*, **9**, 1986 (2016).

59. D. Sebastián, V. Baglio, A. S. Aricò, A. Serov and P. Atanassov, *Applied Catalysis B Environmental*, **182**, 297 (2016).

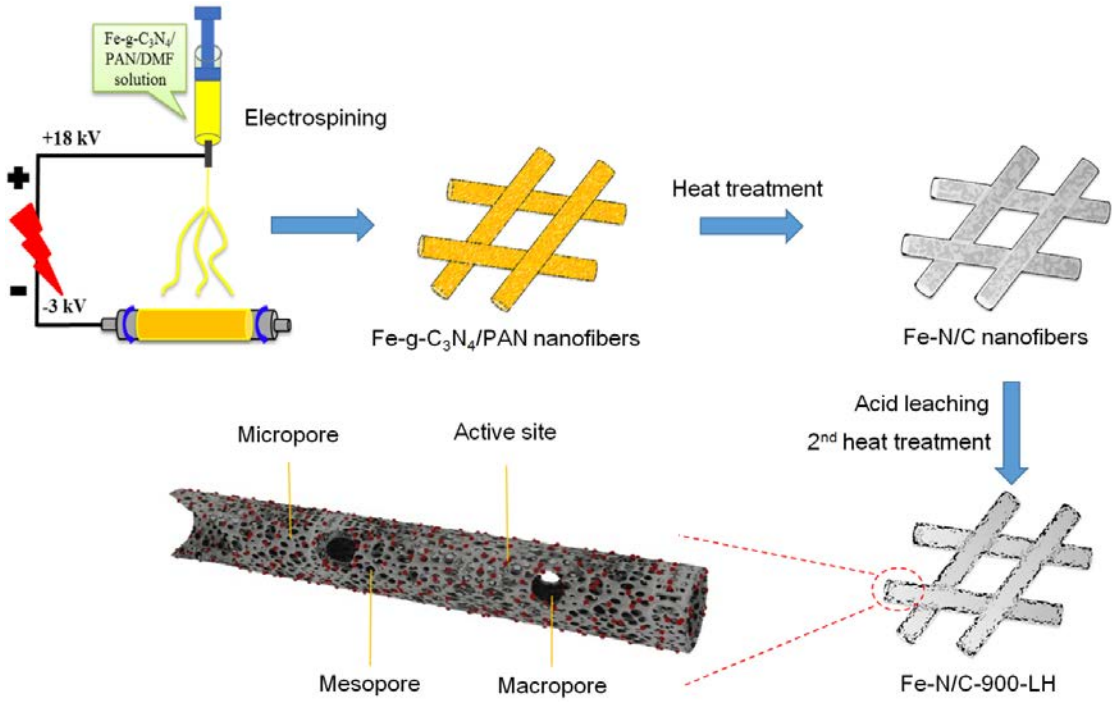

Figure 1. The schematic illustration on the preparation of multi-scaled porous Fe-N/C nanofibers.

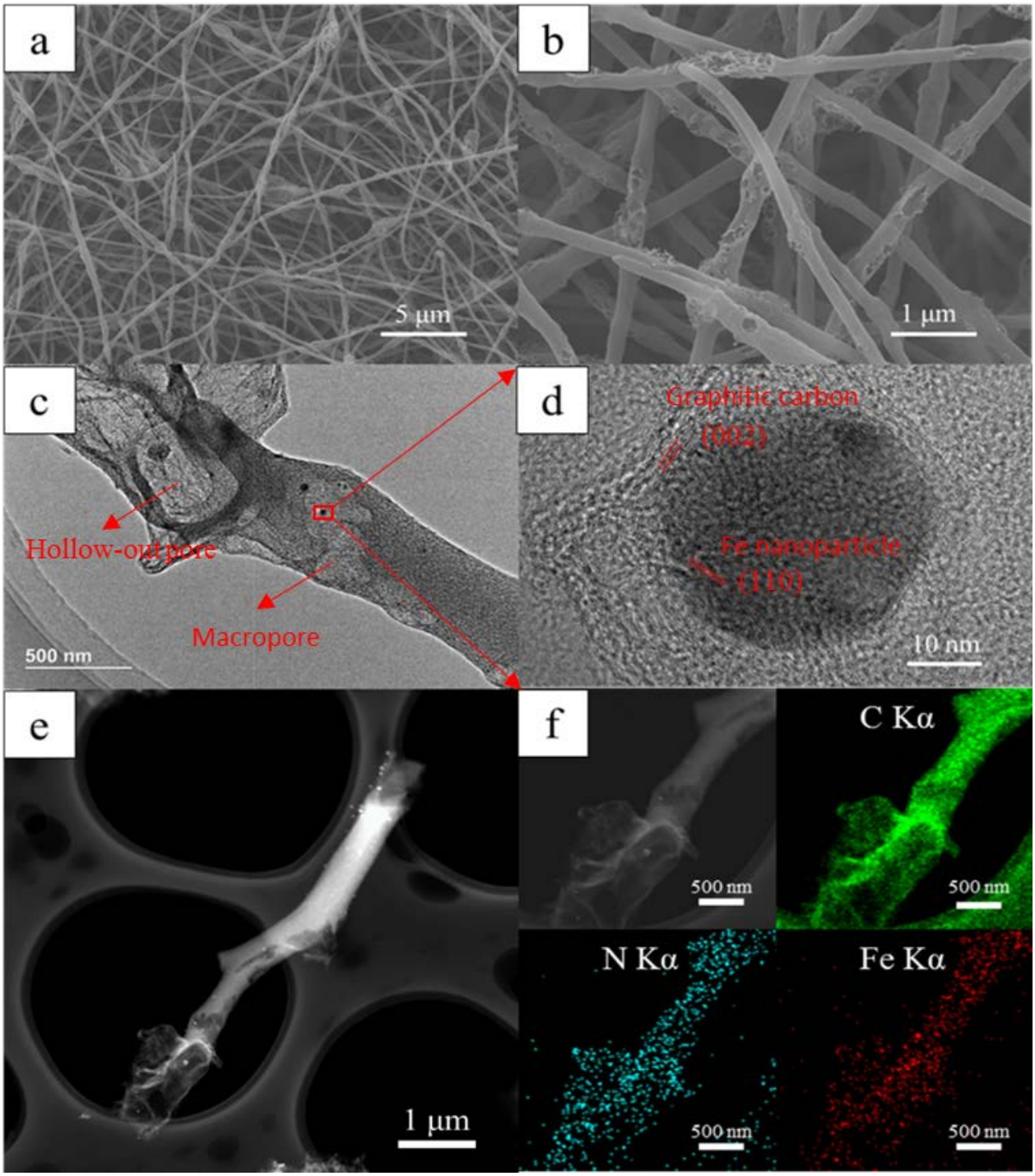

Figure 2. The morphology and elemental distribution of Fe-N/C-900-LH. (a) Panoramic SEM image, (b) magnified SEM image, (c) TEM image, (d) HRTEM image, (e) HAADF-STEM image and (f) STEM image and its corresponding elemental mapping.

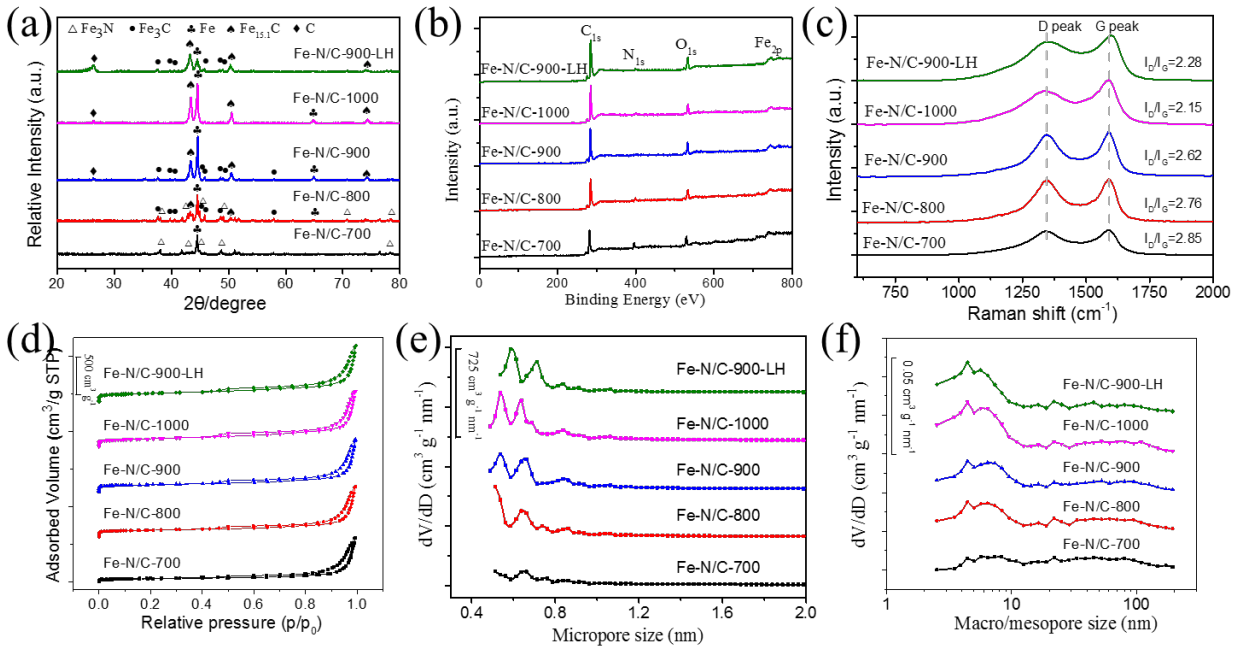

Figure 3. The structure and composition of various Fe-N/C nanofibrous catalysts. (a) XRD patterns, (b) XPS spectra, (c) Raman spectra, (d) N_2 adsorption/desorption isotherms, (e) micropore size distributions and (f) macro/mesopore size distributions.

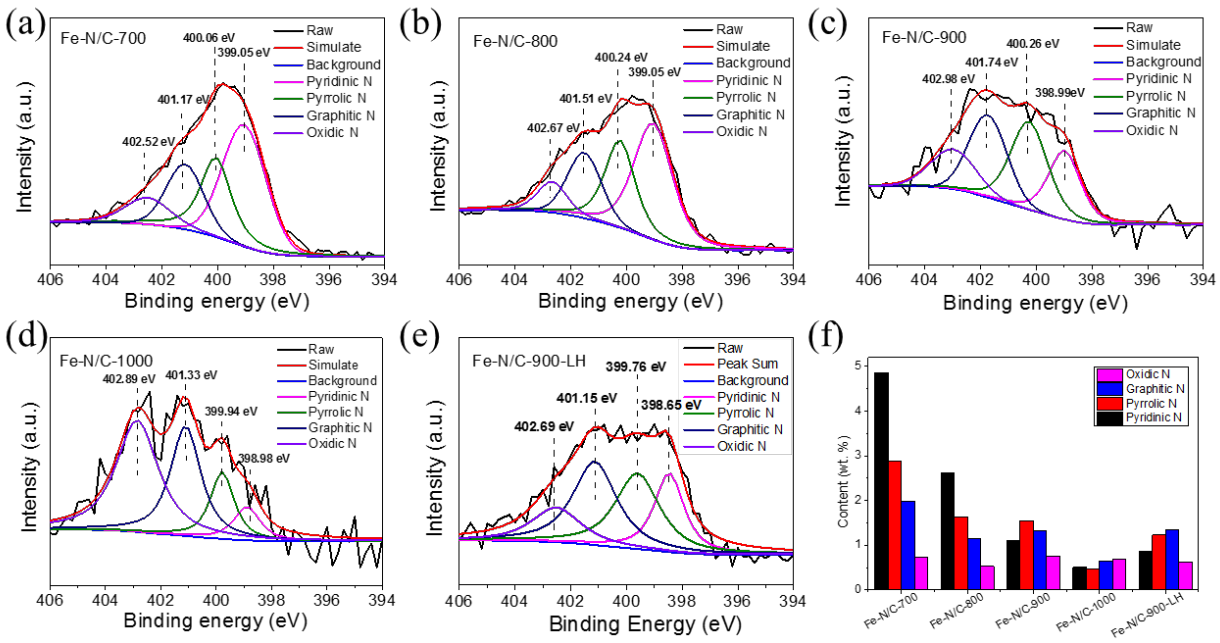

Figure 4. The high-resolution N 1s spectra of various Fe-N/C nanofibrous catalysts: (a) Fe-N/C-700, (b) Fe-N/C-800, (c) Fe-N/C-900, (d) Fe-N/C-1000, (e) Fe-N/C-900-LH and (f) their corresponding contents of different N.

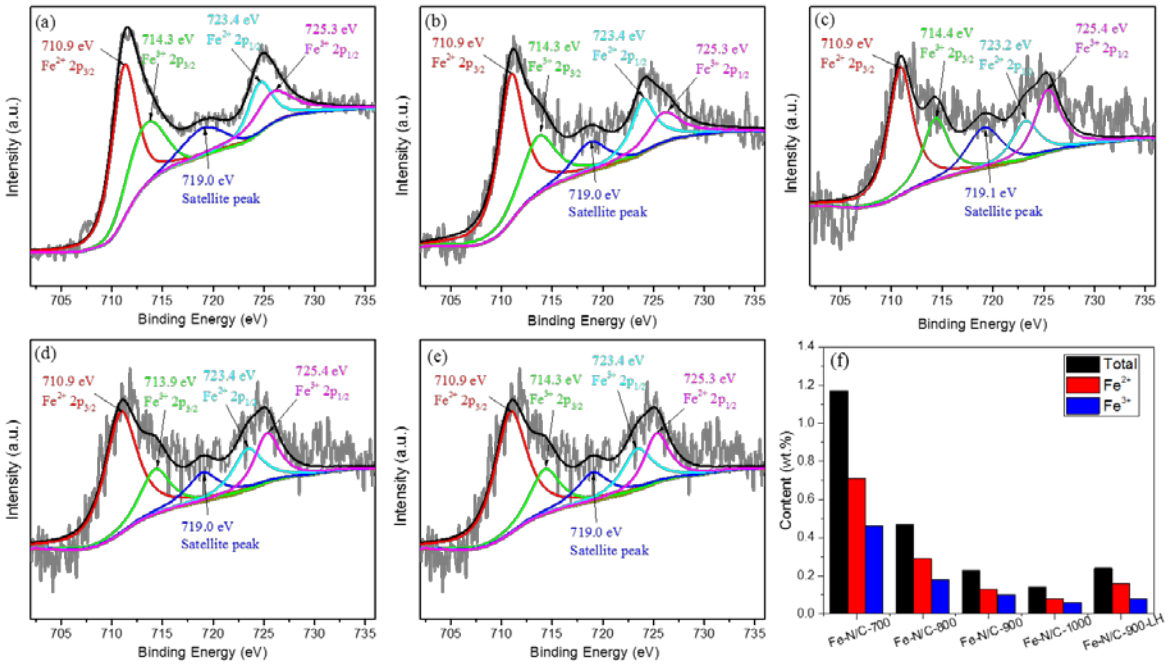

Figure 5. The high-resolution Fe 2p spectra of various Fe-N/C nanofibrous catalysts: (a) Fe-N/C-700, (b) Fe-N/C-800, (c) Fe-N/C-900, (d) Fe-N/C-1000, (e) Fe-N/C-900-LH and (f) their corresponding contents of total Fe, Fe^{2+} and Fe^{3+}.

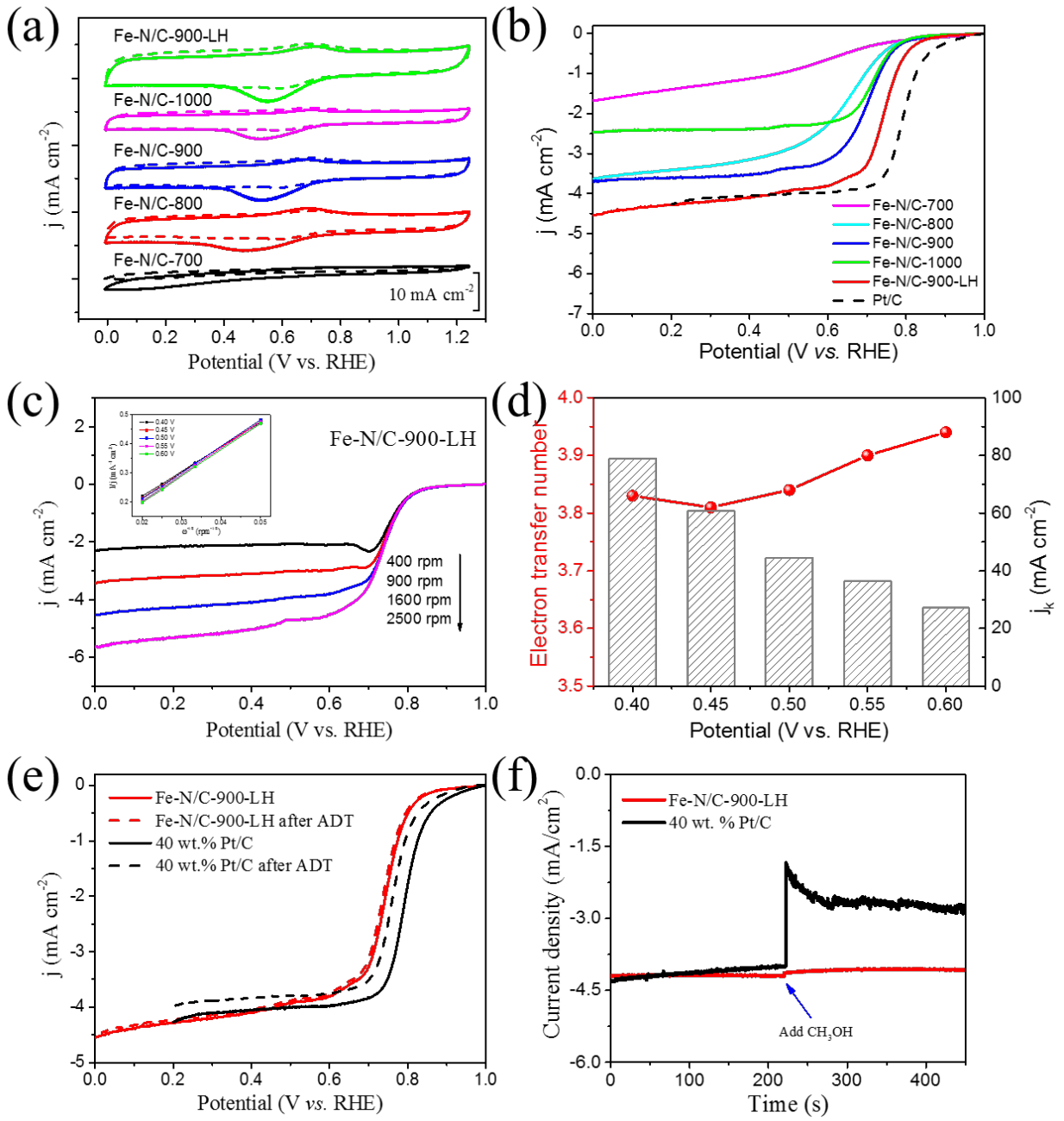

Figure 6. The electrocatalytic characterizations of various catalysts: (a) CV curves of various Fe-N/C nanofibrous catalysts (dash line: N2, solid line: O2), (b) LSV curves of various catalysts at 1600 rpm, (c) a series of LSV curves for Fe-N/C-900-LH, (d) the electron transfer numbers and K-L plots for Fe-N/C-900-LH at different potentials, (e) LSV curves of Fe-N/C-900-LH and Pt/C before and after ADT, and (f) The methanol poisoning tests of Fe-N/C-900-LH and Pt/C.

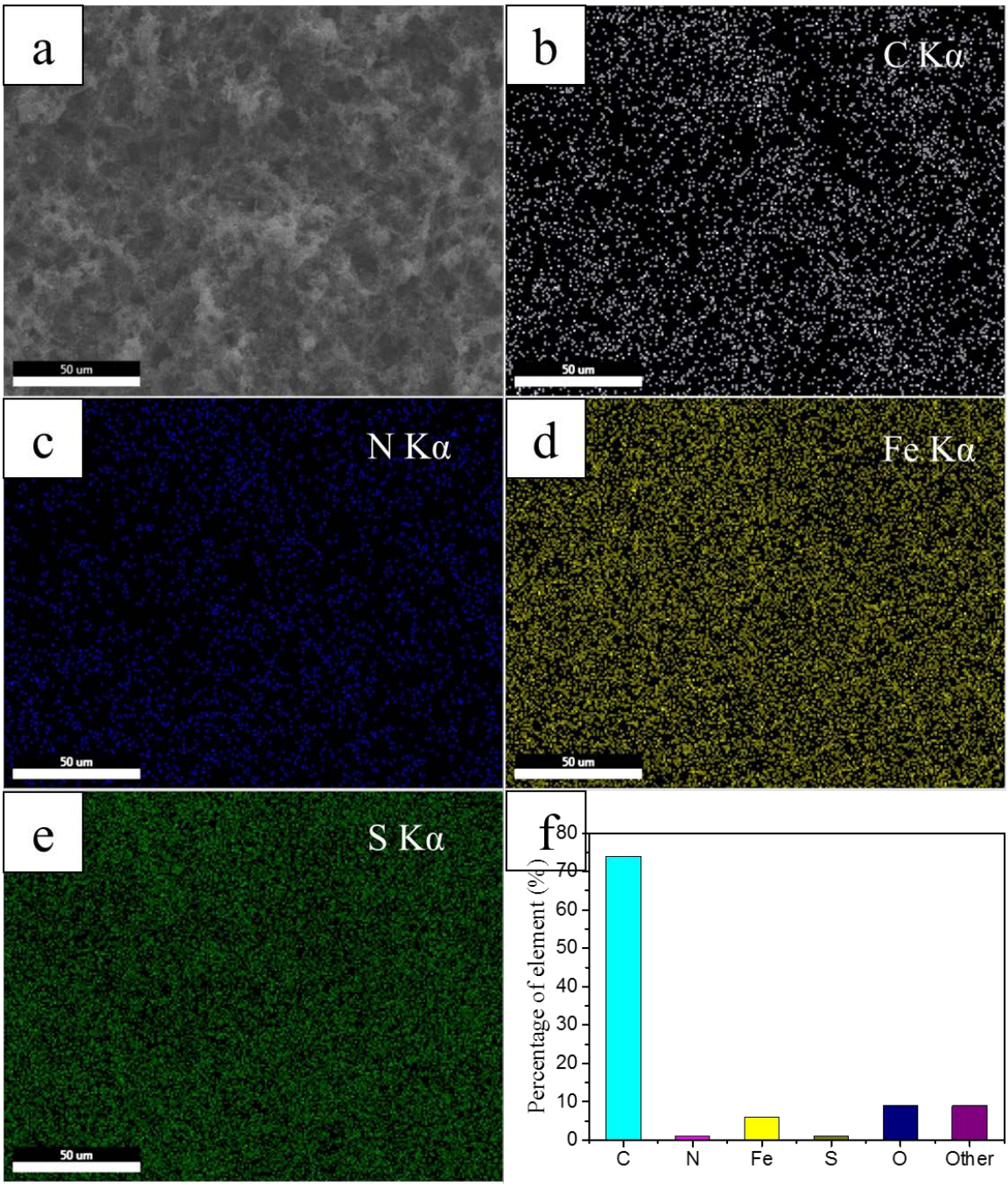

Figure 7. The morphology and composition of cathode catalyst layer prepared by using Fe-N/C-900-LH as the catalyst. (a) The low-magnified SEM image of electrode surface and its corresponding elemental mapping images: (b) C, (c) N, (d) Fe, and (e) S. (f) The content of main elements in the catalyst layer.

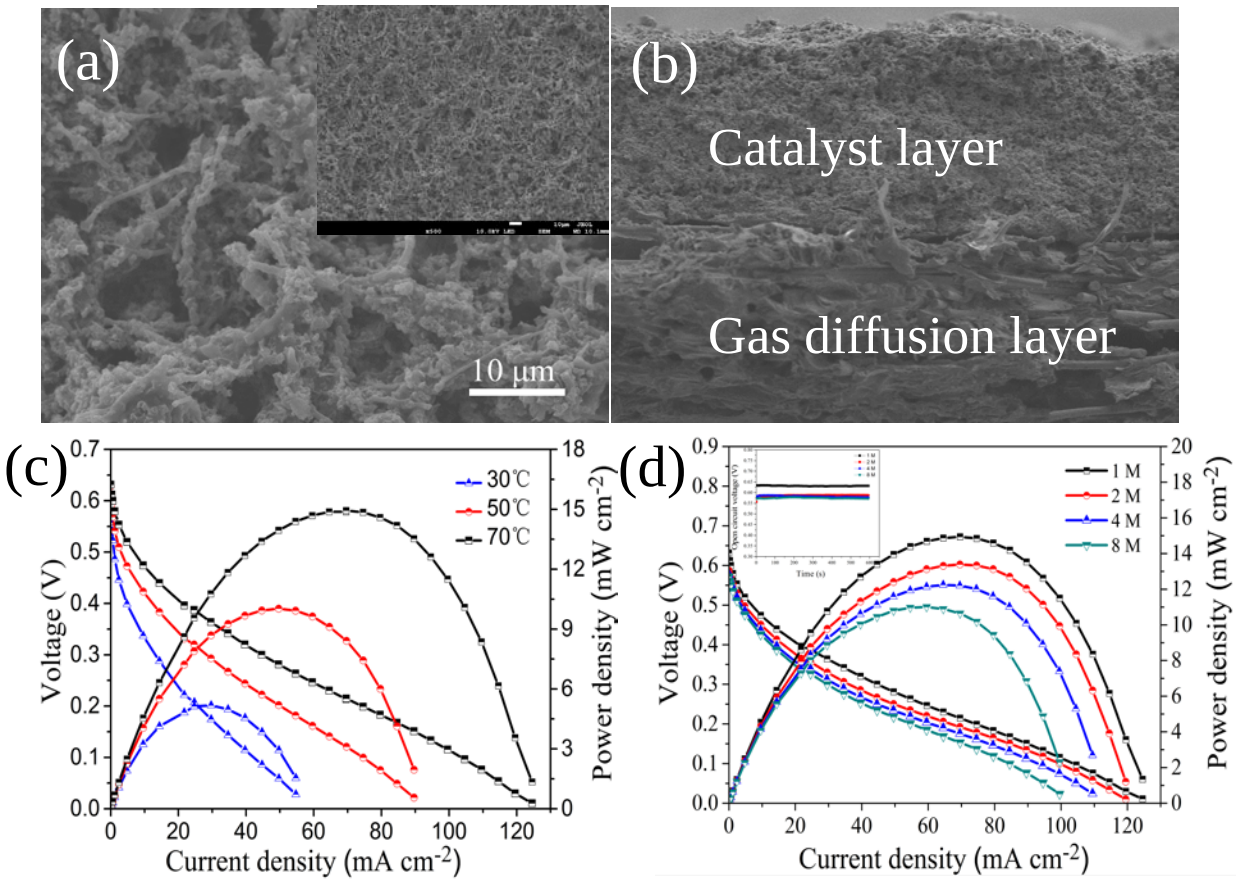

Figure 8. The structure and morphology of cathode electrode prepared by using Fe-N/C-900-LH as the catalyst. (a) The high-magnified SEM image of electrode surface and the inset is its low-magnified image. (b) The cross-sectional SEM image of the electrode. The performance of single DMFC prepared by using Fe-N/C-900-LH as the cathode catalyst: (c) the effect of temperatures and (d) the effect of methanol concentrations.